# Comparison of hexagonal boron nitride and MgO tunnel barriers in Fe,Co magnetic tunnel junctions ⓔ

View Online   Export Citation   CrossMark

H. Lu,[1,2] ⓘ J. Robertson,[1,3,b] ⓘ and H. Naganuma[3,4,5] ⓘ

**AFFILIATIONS**

[1]Engineering Department, Cambridge University, Cambridge CB2 1PZ, United Kingdom
[2]School of Integrated Circuit Science and Engineering, Beihang University, Beijing, 100191, China
[3]Center for Science and Innovation in Spintronics (CSIS), Tohoku University, Sendai 980–8577, Japan
[4]Center for Innovative Integrated Electronics Systems (CIES), Tohoku University, 468-1 Aoba Aramaki, Aoba-ku, Sendai,
 Miyagi 980-8572, Japan
[5]Center for Spintronics Research Network (CSRN), Tohoku University, Sendai 980-8577, Japan

[a]Note: Presented by J. Robertson at the 4th International Symposium for Core Research Cluster for Spintronics, Tohoku University,
Sendai, Japan, February 2021.
[b]Author to whom correspondence should be addressed: jr@eng.cam.ac.uk

**ABSTRACT**

Magnetic tunnel junctions (MTJ) with MgO/Fe based interfaces and out-of-plane spin direction form the basis of present-day spin-transfer-torque magnetic random-access memory (STT-MRAM) devices. They are a leading type of nonvolatile memory due to their very long endurance times and lack of reliability problems. Many semiconductor devices, such as the field effect transistor or nonvolatile memories, have undergone fundamental changes in materials design as dimensional scaling has progressed. Here, we consider how the future scaling of the MTJ dimensions might affect materials choices and compare the performance of different tunnel barriers, such as 2D materials like h-BN with the existing MgO tunnel barriers. We first summarize key features of MgO-based designs of STT-MRAM. We then describe general aspects of the deposition of 2D materials and h-BN on metals. We compare the band structures of MgO and h-BN with their band gaps corrected for the GGA band error. The different absorption sites of h-BN on Fe or Co are compared in terms of physisorbtive or chemisorbtive bonding sites and how this affects their spin-polarized bands and the transmission magneto-resistance (TMR). The transmission magneto-resistance is found to be highest for the physisorptive sites. We look at how these changes would affect the overall TMR and how scaling might progress.

## INTRODUCTION

FETs based on Si/SiO$_2$ interfaces have many advantages in terms of their simplicity, manufacturability, and low power usage, so this basic design has survived many changes of materials arising from Moore's law scaling, from Si channels to SiGe, from SiO$_2$ gate dielectrics to HfO$_2$, from Al interconnects to Cu, and from SiO$_2$ to SiCOH low K dielectrics. The advantage in carrier mobility of 3D semiconductors like
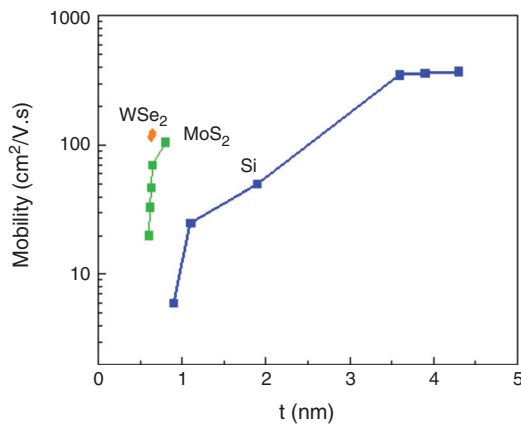
FIG. 1. Electron mobility vs channel thickness (t) for Si conductive channels in an FET compared to that of 2D MoS$_2$ or WSe$_2$ metal dichalcogenide channels in an FET.



FIG. 2. Schematic of the layer structure of the magnetic tunnel junctions. (a) Epitaxial MTJs such as Yuasa et al.[10] and (b) present-day industrial-standard textured stacks with central Co,Fe,B|MgO|Co,Fe,B layers with Co,Fe,B alloy electrodes and interfaces with MgO tunnel barriers. Critical layer thickness in nm are shown in parentheses.

Si over that of 2D semiconductors is now finally being lost, so that 2D semiconductors are now being considered for FET channel thicknesses below ~2 nm[1,2] (Fig. 1). Other 2D materials like hexagonal boron nitride (h-BN) are also being studied for some areas in electronics,[3] such as low K dielectrics by Hong et al.[4] or as the nonlinear dielectrics in resistive random-access memories.[5,6]

This suggests that h-BN could also be considered as a tunnel barrier layer in STT-MRAM, despite what seems as the overwhelming advantage of the present design. MRAM technology is undergoing intense competition against other nonvolatile memory technologies like SRAM, Flash, PRAM, FeRAM, and RRAM in terms of their latency, density, and cost.[7–9] It has succeeded at present due to its very high endurance, low power demand, and high reliability,[8] arising from the absence of atomic motion during operation. However, the ultimate scaling performances in any technology need not correspond to the present-day leader. Recently, the continued scaling of MRAM devices has been analyzed[9] with MgO as the tunnel barrier, but it is interesting to also consider it with h-BN as the tunnel barrier.

## MgO TUNNEL BARRIERS AS AN EXAMPLE

A materials landmark in the development of MRAM was finding that crystalline MgO tunnel barriers gave a much higher tunnel magneto-resistance (TMR) than amorphous Al$_2$O$_3$ due to the presence of the $\Delta_1$ coherent tunneling mode in MgO.[10–12] Yuasa et al.[10] demonstrated a large TMR ratio in Fe/MgO lattice-matched interfaces in full epitaxial stacks grown by molecular beam epitaxy (MBE), as in Fig. 2(a). Patterned FeCo electrodes were found to possess sufficient perpendicular magnetic anisotropy (PMA)[13–15] and MgO|FeCo stacks had enough interfacial PMA[14–17] to orient the spin direction perpendicular to the electrodes, which allowed the continued increase in TMR with decreasing bit size. Another materials landmark was to sputter amorphous Fe,Co,B alloy electrodes between MgO layers and Ta layers, as in Fig. 2(b). Thermal annealing then crystallizes out the MgO, with the B impurity diffusing from the Fe,Co layers to react exothermically with the Ta, which allows the BCC Fe,Co to template out onto the MgO layer in a few-nanometer sized epitaxial grains in a so-called "textured structure."
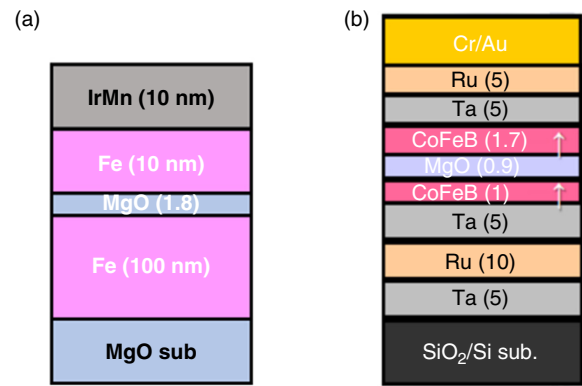
A cross-sectional scanning transmission electron microscopy (STEM) image in Fig. 3(b) shows an assembly of 2–3 nm-sized epitaxial particles of MgO forming a smooth interface by lattice matching in Fig. 3(a). The CoFeB/MgO interface with a textured structure is suitable from the industrial viewpoint, and it is now the de facto standard in MRAM devices.[13,15]

This design benefits from the square symmetry of the FCC MgO (100) interface and the BCC symmetry of the metal over-layer.[10] The cubic symmetry of the MgO tunnel barrier between the electrodes allows its $\Delta_1$ evanescent gap state to dominate the TMR of this barrier, while an earlier amorphous Al$_2$O$_3$ tunnel barrier would mix waves of different symmetry, thus reducing its TMR. The chemical thermodynamics and materials selection of this design are very favorable.[15–17] This allows the energy difference between parallel and antiparallel electrode spin alignments to provide sufficient data retention times. Critical factors here are the symmetry, thermochemistry, and growth mechanisms.[11]
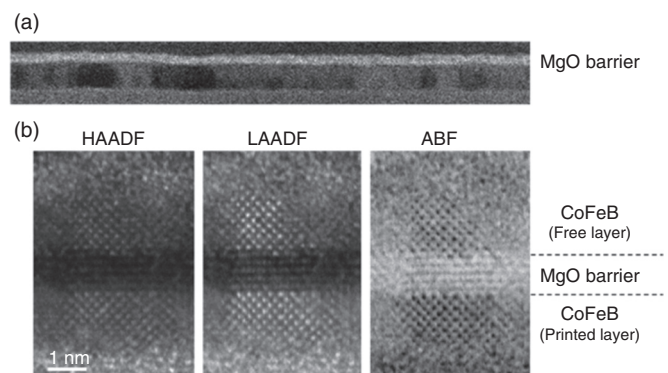


FIG. 3. (a) Scanning tunneling microscope (STEM) images of ferromagnetic textured Co,Fe,B electrode interfaces on MgO tunnel layers. (b) Images showing their abrupt, locally lattice-matched interfaces, under three different STEM imaging conditions; HAADF = high angle annular dark-field, LAADF = low angle annular dark-field, and ABF = annular bright-field images.
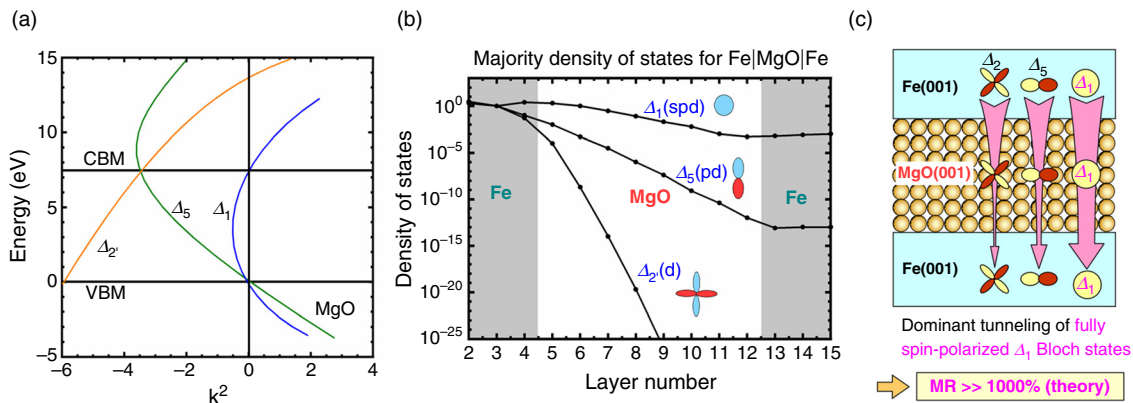
**FIG. 4.** (a). The imaginary band structure of MgO using MgO band parameters,[19] (b) the decay rates of its evanescent states of various symmetries, showing the slowest decay for the $\Delta_1$ s-like state, and (c) schematic of the evanescent states of different symmetries in MgO barriers, showing the slow decay of $\Delta_1$ states, leading to the higher TMR of this symmetry.[11]

The imaginary band structure of MgO can then be calculated as shown in Fig. 4(a). The decay rate of the tunneling states depends strongly on their orbital symmetry around the Fermi level $E_F$, with the s-like $\Delta_1$ states having the slowest decay rate or greatest extent;[18] see Fig. 4(b). The variation of decay rates with their symmetry accounts for the smaller TMR of amorphous $Al_2O_3$ tunnel barriers, as disorder mixes the orbital symmetries in its evanescent states (incoherent tunneling) and causes a faster decay. The replacement of amorphous $Al_2O_3$ by crystalline MgO for the tunnel barriers has led to a rapid increase in TMRs recently.[10–12]

The MgO band structure used to describe the tunneling was calculated in Fig. 5 using the GGA+U method,[19] superseding that of Butler.[18] This adds a potential of $U = 8.5$ eV onto O 2p states to widen the bandgap.[19] This corrects the under-estimated GGA bandgap to
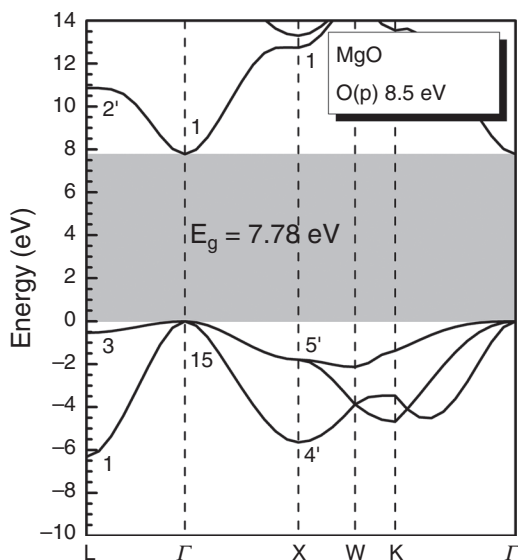


**FIG. 5.** Band structure of MgO by the GGA+U method, giving a corrected bandgap of 7.8 eV.[19]

agree with GW results[20] and also agrees with the experimental electron affinity MgO of $\sim1$ eV.[19]

The most important aspect of the GGA+U results in the context of the present problem is that they correct the bandgap of the insulator (MgO or h-BN), but leave the metal states unaffected. This contrasts with hybrid functional methods like HSE, which are popular for semiconductors. HSE adds a singularity at $E_F$, which works well for semiconductors but causes problems for metallic systems, as seen later in Fig. 13(c).[21]

The design of a local perpendicular magnetic anisotropy (PMA) to align the spins perpendicular to the electrode plane is of great importance. If this arose from an off-stoichiometric interfacial FeO layer at MgO|Fe interface,[22] it would lead to a lower TMR. However, looking at the metal/MgO interface, High-resolution transmission electron microscopy (HRTEM) finds that the Co|MgO interfaces are very abrupt with some interfacial steps. Density functional calculations find that B is insoluble in the adjacent MgO layer.[17] Thus, this system has well-defined interfaces and little interfacial mixing. An electrode of layered alloys like $L1_0$–FePd, FePt, CoPt, MnAl, or MnGa can give a perpendicular PMA for a wider range of thicknesses. However, these alloys are less well lattice-matched to MgO than Fe itself.[10,23]

Theoretically, vertical spins are needed to obtain a cell size of under 30 nm.[15] A number of proposals have considered the orbital interactions at a single Fe,Co interface with those of MgO, as seen in Fig. 6.[24–26] It was found that a convention in-plane easy magnetic axis of FeCoB could be converted into a perpendicular easy-axis by sufficient reduction of the FeCoB thickness to create a buried interfacial perpendicular anisotropy.[14–16]

$$K = K_b - M_s^2/2\mu_0 + K_i/t_{Co,Fe},$$

where $K_b$ is the bulk crystalline anisotropy, which turns out to be negligible, $M_S$ is the saturation magnetization, $K_i$ is the interfacial anisotropy, and $t_{Co,Fe}$ is the thickness of the Co,Fe layer. The dependence is such that K turns positive at $\sim1.5$ nm thickness. Thus, the PMA occurs at very low metal thicknesses of under 1.5 nm.[26] More recently, attention has been paid to the shape and aspect ratio of Fe,Co metal–MgO pillars.[16] The main source of PMA is now the control of aspect ratio of the MTJ stacks where elliptical stacks lead to an
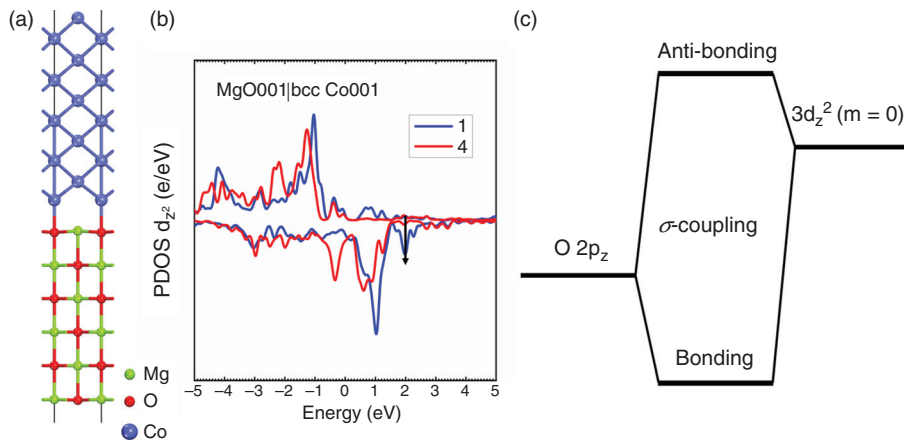
FIG. 6. (a) Atomic model of an abrupt FeCo|MgO(100) interface. (b) Spin-up and spin-down density of states for interfacial MgO layers and Fe,Co planes, showing stabilization of perpendicular metal dz2 states and a model of PMA. (c) Molecular orbital diagram of the interactions.

in-plane magnetic orientation, while circular stacks create a perpendicular magnetic anisotropy.[9]

## 2D MATERIALS AND THEIR DEPOSITION

We now consider whether future scaled MTJ designs could be based on 2D materials such as h-BN. Interest in 2D layered materials such as graphene has often focused on their interlayer van der Waals bonding. Another aspect of most 2D systems is their hexagonal symmetry, which gives their electron states unusual properties at $E_F$ (or Dirac point) at the K point of the Brillouin zone.[27] This occurs because graphene consists of two inter-penetrating A and B sublattices. At K, the two-center $p_z$ interactions between each A to B lattice have exactly zero interaction,[27] so their $\pi$ bands cross each other without perturbation (Fig. 7), leading to their well-known very high carrier mobility. The polar analogue of graphene is h-BN, which has a 5.9 eV bandgap[28,29] and where its valence and conduction band-edges at K are now purely N and B-like, respectively.

The van der Waals bonding gives 2D materials many useful properties such as relatively inert surfaces. However, the absence of surface dangling bonds makes their surfaces problematic for nucleation and growth. For example, graphene does not grow well on non-catalytic surfaces like $SiO_2$[30] while common deposition methods like sputtering of graphene cause disorder and introduce surface charges.

The most viable large-area method of graphene deposition is CVD[31–34] onto a catalytic surface, typically a transition metal. The metal's catalytic ability follows a volcano plot.[35] Considering the overall balance of partial reactions, the catalytic ability requires relatively weak catalysts, otherwise the slowness of leaving species reaction leads to a saturation of the surface sites. Graphene growth follows a process of addition to the dangling bonds on the edges of surface graphene islands, so that full surface coverage can require long deposition times.

Copper is a favored catalytic substrate for graphene growth, being moderately catalytic, but its volatility is a problem for the high temperatures used to limit deposition times. Higher temperature also causes carbon to dissolve interstitially in the substrate. Cooling the substrate then precipitates out the dissolved carbon on its surface as multilayer graphene. If a more effective catalyst like Fe is used, carbon has a higher solubility in Fe, and forms metastable carbide precipitates, allowing even higher effective solubility. This leads to growth of multilayer graphene by precipitation, but often in a less controllable way.
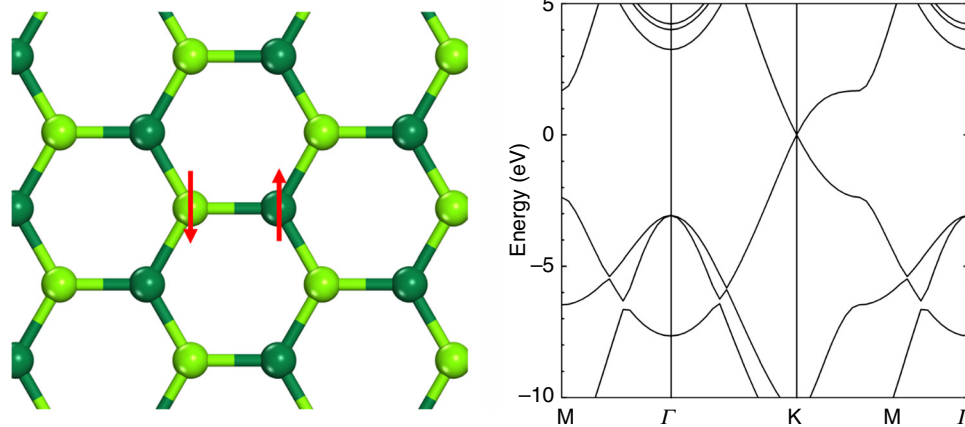


FIG. 7. Graphene, showing its two hexagonal sub-lattices and their band structure around the Dirac point with their band crossing at $E_F$.

Thus, many workers favor Cu. Large area (200 mm) graphene CVD is possible using copper on SiO$_2$ deposited on Si wafers[33] and by roll-to-roll deposition.[34]

Attention then turned to 2D semiconductors such as MoS$_2$ for FET applications. The lattice of MoS$_2$ is also hexagonal. MoS$_2$ has an indirect gap that becomes direct when it is reduced to a monolayer.[36] CVD again is the preferred large-area growth method, but it should be used on insulators if the intention is to make an FET. The problem with MoS$_2$ CVD is the large difference in sticking coefficients of the Mo and sulfide precursors required for optimum deposition. Growth occurs by the incident species sticking weakly to the islands, diffusing laterally across the islands, and then adding onto the island edges. The islands then grow laterally until they make contact with each other, as shown in detail by Robinson *et al.*[37] The shape of each growth island similar to that Fig. 8 is not the most simple and causes some difficulty in forming a uniform coverage.[38] It takes extended times to fully cover a surface. Each layer of growth must be nucleated separately.[38] Chiappe[39] showed successful deposition of large area CVD samples.

MoS$_2$ is essentially an n-type semiconductor with a dominant defect, the S vacancy, which forms states in the upper bandgap, making it n-type.[40] A comparison between the chalcogenides finds that WSe$_2$ is a more ambipolar semiconductor with anion vacancy level lying near midgap.[40] This makes WSe$_2$ a more favored 2D semiconductor than MoS$_2$, but it is less well investigated. The effect of electrical contacts and Fermi level pinning by interface states, vacancies, and impurities has been extensively studied in MoS$_2$ for electrical applications.[41–43]

## h-BN AND ITS DEPOSITION

h-BN is a wideband-gap layer compound which presently finds its major use as a flat substrate to maximize the electrical conductivity of graphene.[44] It can also act as a tunnel barrier in MTJs.[45] Its deposition conditions are similar to those of graphene, using transition metals like Fe, Co, Ni for catalytic growth.[45–50] The preferred BN precursor is borazine, B3N3H6. Small crystallites of h-BN tunnel barrier material for MTJs have been grown on Fe and Ni surfaces at $\sim$900 °C. The overall CVD growth of h-BN is similar to that of graphene, with outward growth from island nuclei and high degrees of surface coverage
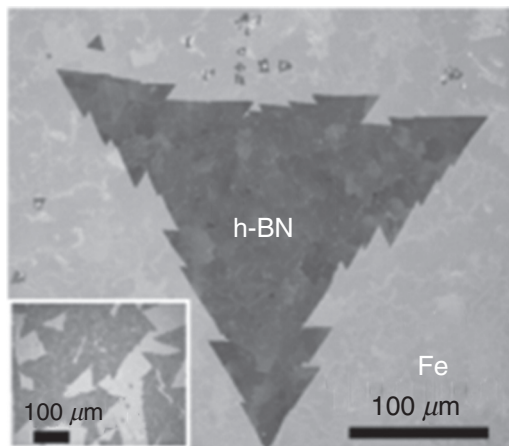


**FIG. 8.** The growth mode and surface coverage of monolayer h-BN on Fe, showing the difficulty of uniform coverage (private communication, S. Hofmann, 2018).

requiring long growth times. The unusual growth shape (Fig. 8) arises because the growth species must diffuse and then attach to the nearest island. Similar growth shapes are found also for graphene.

Multilayer h-BN can be grown at higher temperatures ($\sim$1100 °C) than for monolayers, using precipitation from the metal, as seen by Kong *et al.*[51] B is an interstitial and has a moderate solubility, whereas N is much less soluble and is mainly surface bound.[45] This means that the h-BN interfaces with metals are formally abrupt, but the surface solubility of interstitial B can be significant.

h-BN can also be deposited by sputtering or evaporation, but this causes disordered networks and charged defects. Thus, CVD is presently the preferred option and restricts useful alternatives such as sputtering. Atomic layer deposition (ALD) is often a favored method for layered systems but has only recently been used for h-BN, using precursors such as NH$_3$ and BCl$_3$.[52–56] Recent ALD work has been found to create well-ordered h-BN networks with few like-atom bonds, as seen by their XPS core spectra.[52] ALD has the advantage of a lower growth temperature ($\sim$600 °C) than CVD, which implies lower h-BN solubility in the substrate surface. Growth temperatures down to 330 °C have been achieved,[54] which is compatible with back-end-of-line processes.

The absence of network disorder is an important consideration, given that the lower TMR of a-Al$_2$O$_3$ led to its replacement by MgO. The preference for ordered or disordered networks follows the bond ionicity. Naguid and Kelly[57] found that quenching a disordered phase produces a crystalline or amorphous phase depending on whether the ionicity exceeds roughly $\sim$0.50 or not. This arises because the relative cost of like-atom bonds rises with increasing ionicity. h-BN has an ionicity of $\sim$0.26, while MgO is 0.84. h-BN is considerably less ionic than Al$_2$O$_3$. Al$_2$O$_3$ is stable as an amorphous phase, but this may be unusual, given its ionicity is $\sim$0.79.[58]

Grain boundaries in isolated h-BN films are found by TEM to contain many 5–7 membered rings with B-B and N-N bonds,[59] which show that like-atom bonds are energetically possible in isolated h-BN or with a low dielectric constant substrate. On the other hand, grain boundaries in h-BN films attached to a more conducting substrate have a preference for even-membered rings.[60] This shows that h-BN films screened by a metal layer favor networks with 8–4 rings, distorted bond angles but fewer wrong bonds over 5–7 rings. Molecular dynamics can create a random network of h-BN like that of glassy carbon with many odd-membered rings;[61] see Fig. 9.

The ALD reaction of NH$_3$ with BCl$_3$ to form h-BN is effectively

$$NH_3 + BCl_3 = BN + 3\,HCl.$$
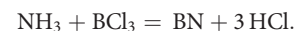
So, the formation of each B-N bond is also accompanied by an exothermic formation of H-Cl bonds. The effect of this extra reaction is to increase the effective ionic energy of B-N by the addition of three HCl contributions as well. Thus, the effective ionicity of BN during an ALD process is effectively doubled, from 26% to $\sim$60%, so that the ordered phase becomes much more favored in the Naguib and Kelly model.[57] Thus, although ALD h-BN might not be very crystalline, it might have sufficient short-range order to favor coherent spin tunneling. This then allows the lower ALD growth temperatures.

## BONDING SITES OF h-BN ON Ni, Co, Fe SURFACES

h-BN has a good lattice-match to the (111) surfaces of the three magnetic metals Fe, Ni and Co, taken in the fcc structures.[62–64] h-BN
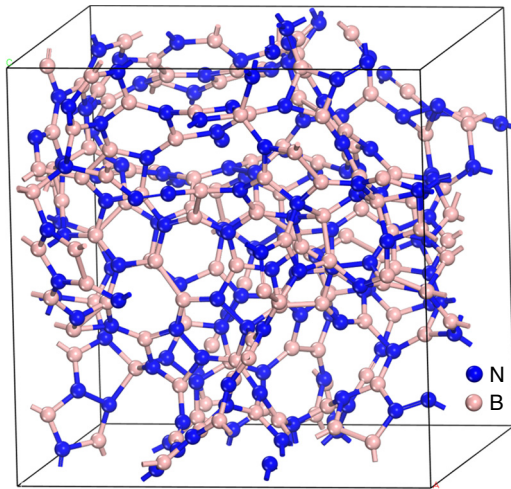
**FIG. 9.** Random network of h-BN calculated by *ab initio* molecular dynamics (pink = B, blue = N).[61]

can adopt three different bonding sites on (111) Ni surfaces in density functional (DFT) calculations: the metal on N-top, B-top, and in the incommensurate $\sqrt{7} \times \sqrt{7}$ structure,[62–65] as seen in Fig. 10(a)–10(c). The "N on top" site is the most stable by 0.25 eV; it is a chemisorptive site with a metal-N bond length of 2.15 Å in which the occupied N $p_z$ states interact with the metal states directly below. The "B on top" is a less preferred physisorptive site with a B-metal bond length of 3.22 Å
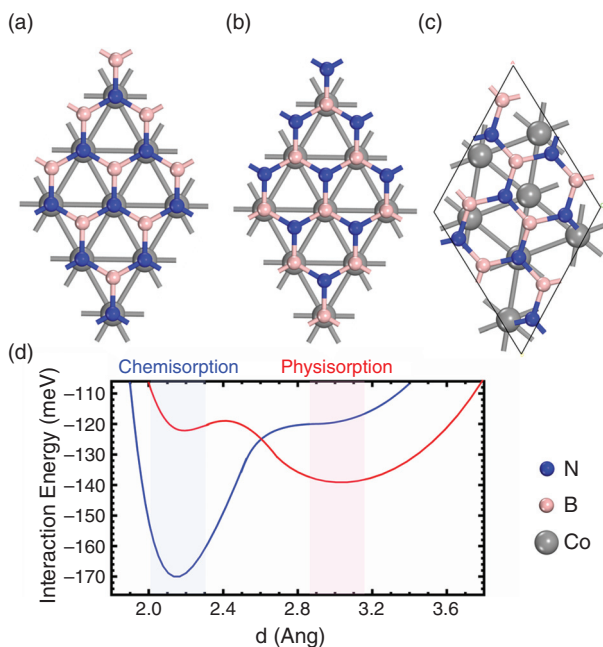


**FIG. 10.** (a) The three configurations of h-BN on (111) faces of Co or Ni, N on top, B on top, and an incommensurate $\sqrt{7} \times \sqrt{7}$ structure, involving a small rotation. (b) Binding energy per formula unit of h-BN on **Ni**, at the chemisorbed N on-top site and of the physisorbed (incommensurate) structures, after Ontaneda *et al.*[64]

where the empty B $p_z$ states interact more weakly with the metal states. This is another physisorptive site with a $\sqrt{7} \times \sqrt{7}$ structure with a B-metal separation of 3.25 Å in our calculations. This consists of 25% of of nearly 'N-on-top sites' and 75% of bridge sites, Fig. 10(c), The chemisorptive and physisorptive sites have different energy vs distance dependences, as seen in Fig. 10(b), which also depend slightly on the interatomic potentials. The $\sqrt{7} \times \sqrt{7}$ site has not yet been confirmed experimentally to have long range order. Note that h-BN has higher modulus than Ni, and it is likely to constrain the matching.

## CALCULATED ELECTRONIC STATES OF h-BN

The bands of bulk h-BN have been calculated by the GGA method with a cutoff energy of 300 eV, using plane-waves and ultrasoft pseudopotentials by the CASTEP code (Fig. 11). An empirical van der Waals interaction in the Tkatchenko-Scheffler scheme[66] is included for the interlayer interaction. The overall calculation is converged to an energy of $10^{-6}$ eV per atom and to forces of under $10^{-4}$ eV/Å. However, as is well-known, the GGA method underestimates the bandgap from 5.9 eV to 4.27 eV.

Figure 11 also shows the h-BN band structures found by other means. We include the more costly HSE hybrid functional method, with a fraction $\alpha = 30\%$ of Hartree-Fock exchange added to the density functional to correct for the GGA bandgap error of h-BN. These bands compare well to the GW bands[28,29] and the sX bands.[67] We also show in Fig. 11 the bands given by the recent lower-cost GGA+U method, following the ABCN method, where on-site potentials of $U(N,p) = 6.5$ eV and $U(N,s) = 6$ eV are added to the N potential within GGA to give a corrected bandgap. It uses a plane wave cutoff of 400 eV. Figure 11 shows that the GGA+U bands of bulk h-BN are similar to those found by HSE. The GGA+U method is useful as it has a similar low cost as GGA, so that the GGA+U method can be useful for systems with the more complex structures such as the $\sqrt{7} \times \sqrt{7}$ incommensurate structure shown in Fig. 10(c). Figure 11 also shows the corrected bandgap from the LCAO h-BN scheme used later in the supercell TMR calculation.
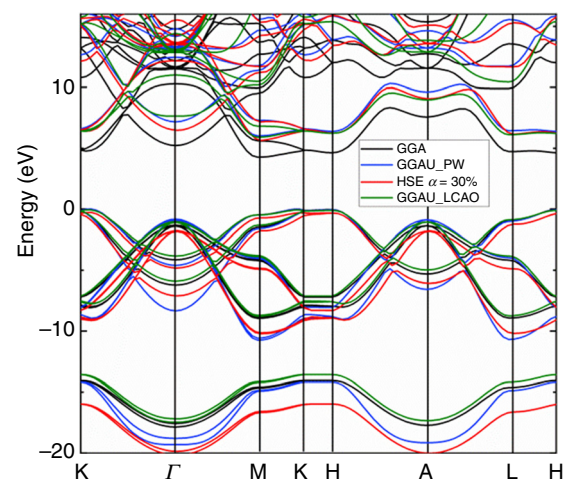


**FIG. 11.** Band structure of bulk h-BN, by the GGA, GGA+U, HSE, and LCAO methods, aligned to the valence band maximum at K.

The band structure of h-BN is unusual in that the $p_z$ band edge states at the K point are both 100% ionic, which arises from the two sublattice structure of h-BN. There is also the unusual conduction band with a local minimum at $\Gamma$, which arises from localized interlayer states.[29] This occurs in bulk h-BN (and graphite) calculations, but it is not found in the minimal basis set treatments.[68] This minimum is less pronounced in the monolayer case.

Figure 12 shows the spin-polarized bands of supercells of h-BN on Co(0001) by the various methods. There are five layers of Co for each electrode, five layers of h-BN per supercell, and no vacuum gap. Here, a $7 \times 7 \times 2$ k-point scheme in the primitive cell is used for structural relaxation in GGA, while a $2 \times 2 \times 1$ k-point scheme is used for the $\sqrt{7} \times \sqrt{7}$ cell. The h-BN layers are relaxed in the N-on-top position on Co, for a short chemisorption bond length of 2.15 Å. The GGA bands for the N on top site are seen in Fig. 12(a).

We see that the GGA+U method opens up the local gap of the h-BN, shown as black bubbles in Fig. 12(b) compared to Fig. 12(a). Also, the Co-based bands are barely changed from the GGA bands, so that the GGA+U metal bands retain the energy and k-vector dependence seen in the simpler GGA form. Thus, the GGA+U bands combine the good features of both the h-BN bands and the Co bands.

Figure 13 shows the spin-polarized PDOS for the GGA and GGA+U bands, corresponding to the bands of Fig. 12. This shows that the metallic bands around the gap region are very similar around

$E_F$ and in the bandgap of h-BN. The U within the GGA+U bands has opened up the gap within the GGA+U bands of the h-BN component without affecting the metal-like bands. On the other hand, in Fig. 13(c) HSE enlarges the bandgap of the h-BN component, but it completely distorts the underlying PDOS of metallic states from $-4$ eV to $+2$ eV. This behavior may be unfamiliar to those with a semiconductor background. However, the HSE bands contain a component of Hartree-Fock exchange that creates a singularity in metallic PDOS at $E_F$. Thus, the HSE treatment should not be used for metallic systems like an MTJ.[67]

Figure 14(a) compares the GGA+U PDOS for the chemisorbed N-on-top configuration to that in the physisorbed B on-top [Fig. 14(b)] and the $\sqrt{7} \times \sqrt{7}$ configuration [Fig.14(c)], where the physisorbed sites both have the longer Co-BN layer van der Waals separations. We see that the Co PDOS in Fig. 14(b) is similar to those in Fig. 14(a), while the h-BN PDOS has been shifted to lower energies for the physisorbed $\sqrt{7} \times \sqrt{7}$ site, which has too many bands to be shown in a band diagram. On the other hand, the PDOS for the two physisorbed configurations, B on top and the $\sqrt{7} \times \sqrt{7}$, are quite similar.

Figure 15 plots the valence band offsets (VBOs) (or p-type Schottky barrier heights) of the h-BN against the $E_F$ of Co derived from Fig. 12. The Co Fermi energy in the GGA+U bands is higher in the gap compared to its energy in the GGA case. This gives a larger VBO between the h-BN valence band edge and the Co Fermi energy



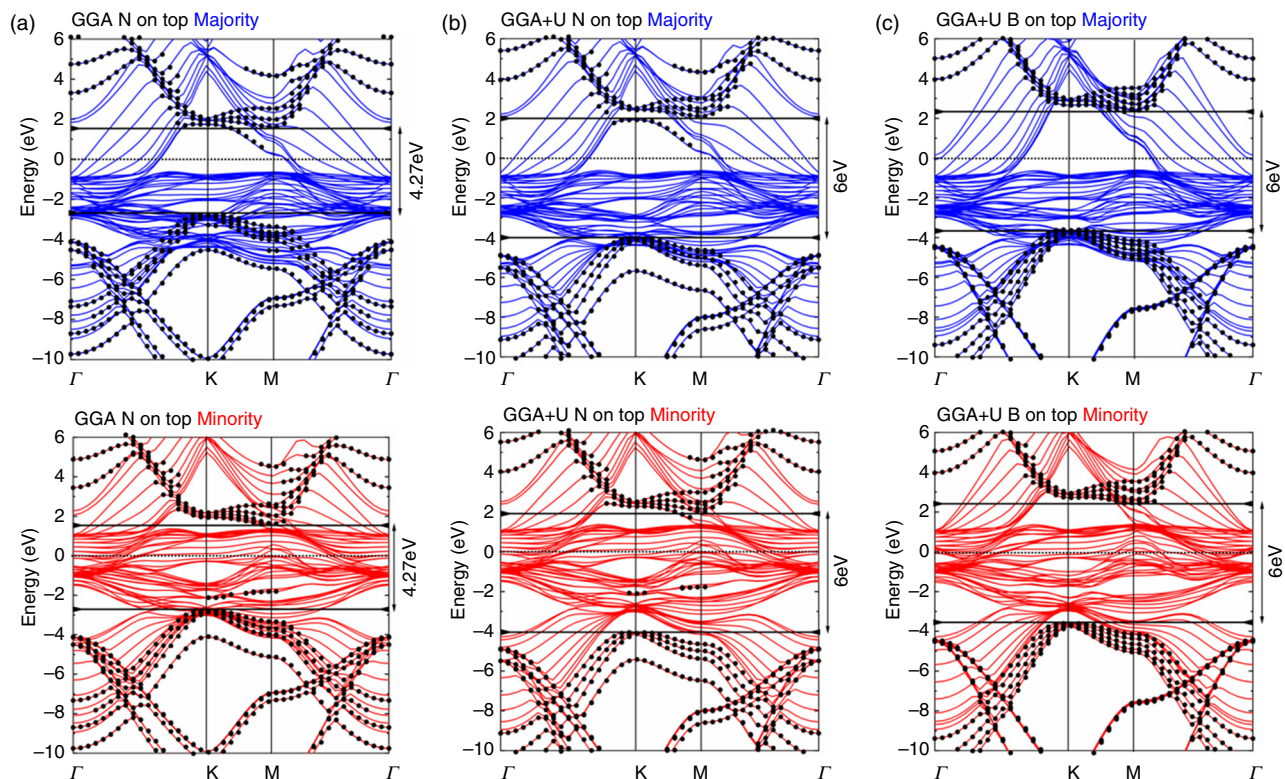**FIG. 12.** Spin-polarized band structures of (0001) Co|h-BN|(0001)Co multilayer supercells, by (a) GGA, and (b) GGA+U methods for the chemisorbed N-on-top geometry; (c) physisorbed B-on-top geometry for illustration. The gap of the projected h-BN bands is shown by arrows. Metal Fermi energy = 0 eV. Black dots are BN-like bands. Note absence of Co-like spin-up states near K-M at $E_f$, as in spin filtering.
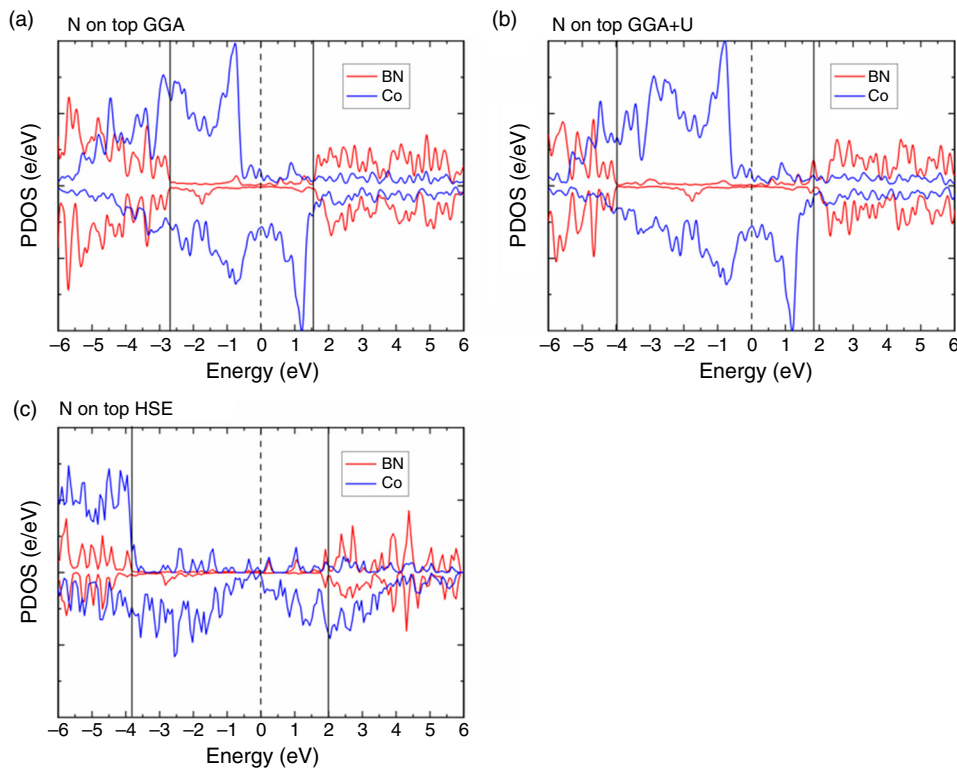
**FIG. 13.** Comparison of (a) GGA and (b) GGA+U PDOS for chemisorbed h-BN for the N-on-top Co state. Vertical lines at h-BN band edges. Note the widening of the h-BN bandgap, while retaining the similar Co PDOS in the GGA+U method. (c) PDOS by the HSE method. Note the widening of the h-BN gap, but also the large distortion of the Co PDOS between −4 eV and 2 eV caused by the Hartree-Fock component of HSE, which led to our discontinuing using it for this application.

of 4.0 eV in the GGA+U case (within band gaps of 5.9 eV), rather than a VBO of 2.7 eV found in GGA (for a 4.7 eV bandgap). It also shows the band offsets based on the experimental electron affinity of h-BN of −0.5 eV[69] and the work function of Co of 5.0 eV. These band calculations can be compared to recent angle resolved photoemission (ARPES) data of Usachov.[70]

These results indicate an unusual shift of the h-BN to Co band offsets with their layer separation. This is a general effect. Although the energetic stabilization of the chemisorbed bond length (∼2.15 Å) compared to the physisorbed bond length (∼3.25 Å) is only small (∼25 meV/FU), it has a major effect (∼2 eV) on the Schottky barrier height between the Co and h-BN layers in the chemisorption regime due to an exchange-repulsion effect or pillow effect.[71–73] The movement of the closed shell h-BN layer into the metal cannot create a charge transfer dipole between the h-BN and the metal because of the large h-BN bandgap. However, it can create a polarization within the metal charge density due to the exchange hole, which shifts the metal $E_F$ uutward by up to ∼2.5 eV as shown in Fig. 16 and is explained in detail by Bokdam et al.[65] Thus, $E_F$ appears quite high in the gap for chemisorbed metals like Ni, Co, and Fe.

However, if the Co-N separation increases to the van der Waals length, $E_F$ moves lower in gap, nearer to the h-BN VBM, as in, for example, the GW bands of Faleev[74] (which used the incorrect physisorbed bond length for the N-on-top structure). Thus, the h-BN layer can be moved to the physisorption distance either by changing to the √7 structure (as in Fig. 14) or by manually increasing the Co-N distance in the 1 × 1 structure. The pillow effect is the same effect that causes dipole shifts in the SBHs for metal organic molecule interfaces.[71]

A final unusual effect for chemisorbed structure is that for this Co-N bond length, there is a rather strong bond between Co and the top h-BN layer (layer 1) but still a weak bond between layer 1 and layer 2. Thus, layer 1 has a different SBH to that found for the remaining h-BN bands, labeled $\phi_P$ and $\phi_P*$ in Ref. 65.

It should also be noted that the metal d bands do not appear in the h-BN bandgap where expected from the h-BN electron affinity value of Ref. 69, in Fig. 15. This large valence band offset between the h-BN VBM and the Co $E_F$ within GGA+U method means that only states around $E_F$ are relevant for tunneling in the MTJ, and those nearer VBM using the erroneous GGA method are unlikely to contribute to tunneling even under an applied voltage, as suggested in Ref. 74. The spin-down HSE bands show an absence of states around $E_F$ near the K point, as noted in the spin filtering mechanism.

## MAGNETO-TUNNEL RESISTANCE OF H-BN|METAL JUNCTIONS

We now consider more experimental details of h-BN as a tunnel barrier.[75–79] In a recent study, h-BN was grown first on Ni by CVD. Then, a top Ni electrode was then evaporated onto the h-BN layer at room temperature.[76] This meant that the lower interface had the Ni-on-top chemisorption configuration with a short bond length to the metal, whereas the upper interface had a √7 physisorption configuration, with the long bond length to the metal. The TMR of hBN sandwiched between these two electrodes was measured as a function of the voltage between the two electrodes and it was found that the TMR changed sign with voltage,[76] in agreement with a DFT model of spin transport across the sandwich.

(a) N on top GGA+U

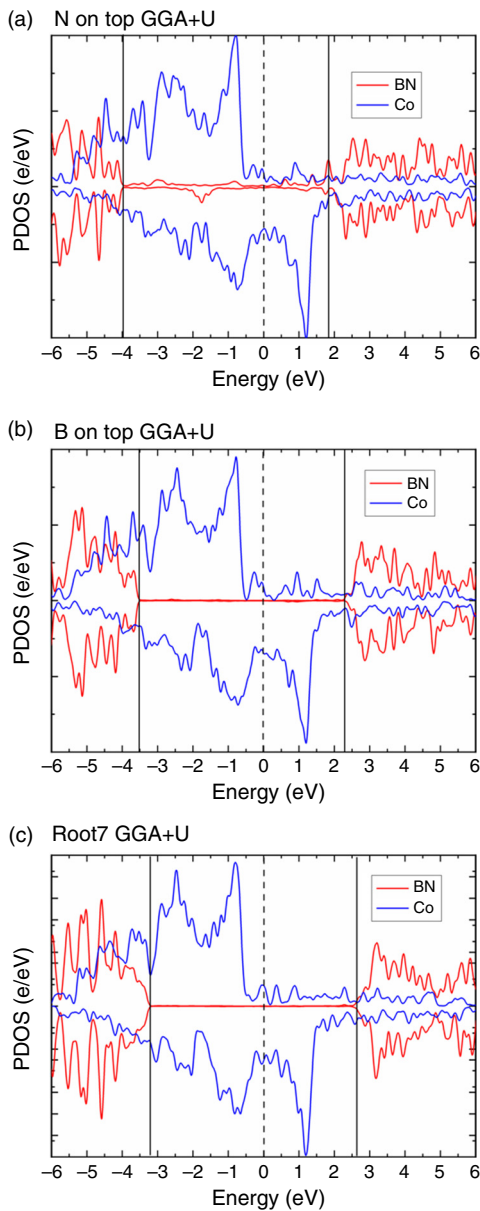(b) B on top GGA+U

(c) Root7 GGA+U

**FIG. 14.** Comparison of the GGA+U PDOS for (a) the N-on-top chemisorbed site, and the two physisorbed sites of h-BN on Co, (b) the $\sqrt{7} \times \sqrt{7}$, and (c) B-on-top site.
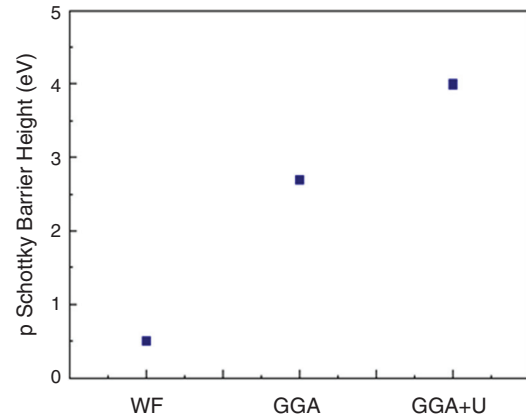


**FIG. 15.** Schottky barrier height (valence band offset) between the valence band maximum of h-BN and the Co Fermi level in the N-on-top MTJ supercell, for the different calculation methods (a)–(b), compared to (c) an experimental value estimated from the Co work function (WF) and the h-BN electron affinity.

dependence of the decay rate with energy was less important.[19] In contrast, in hexagonal BN there is a strong "spin-filtering" dependence on k vector, that is a blocking of tunneling if an electrode has no available states of the desired K vector and spin polarization to receive the tunneled state.[80–82] The decay rate of evanescent states in h-BN depends quite strongly on their energy, but has a weaker dependence on orbital symmetry, unlike MgO. The s*-like $\Delta_1$ state (blue) has the lowest decay constant in h-BN for much of the gap, rather than a s-like state as in MgO. The next lowest decaying state near the gap center is another $\Delta_1$ state at K (green) with $p_z$ orbital symmetry.

The tunneling transmission spectra for the GGA+U bands have been calculated for the case of the N-on-top bonding configuration and 5 h-BN layers between Co electrodes, as shown in Fig. 18(a). The spectra show some spikes due to the frequent band crossings. From these, we calculated the TMR spectrum for the junction on a logarithmic scale in Fig. 18(b).

The average TMR value in the gap on the logarithmic scale is around 200%, but it does fall just above $E_F$. This means that the h-BN

## CALCULATED MAGNETO-TUNNEL RESISTANCE OF h-BN|METAL JUNCTIONS

The tunneling states of h-BN are related to its imaginary band structure as shown in Fig. 17. These bands have various branches, including $\Delta_1$ states connecting the $p_z$ band edge states at K in green, and the $\Delta_1$ states connecting the s,p$\sigma$ valence to the s* interlayer conduction band minimum state at $\Gamma$(blue).[74]

We noted earlier that the decay rate of the evanescent states in cubic MgO varies strongly with their orbital symmetry, and the
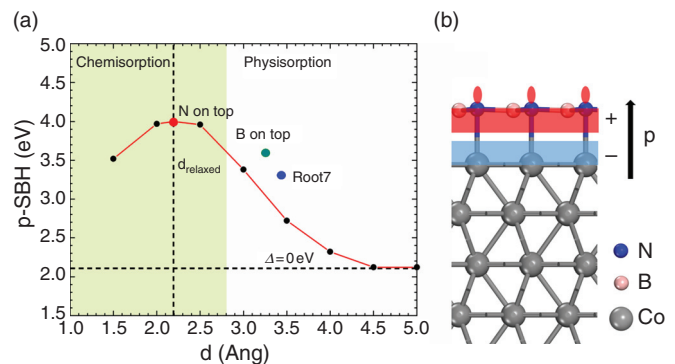


**FIG. 16.** (a) Energy of the metal Ef vs from the hBN valence band energy as a function of the h-BN layer to metal surface. The top of the curve is for the chemisorption distance. (b) Charge density dipole of h-BN layer pushing into the metal layer, or 'pillow effect', as in Ref. 71.
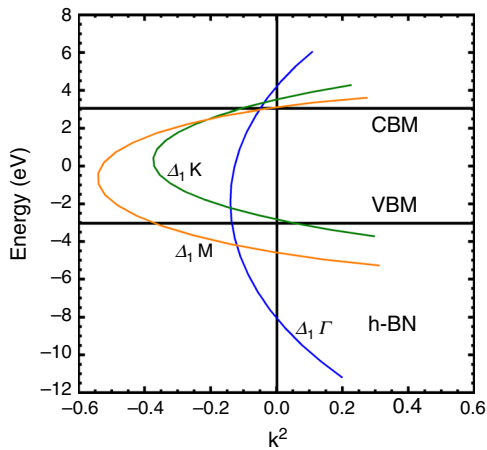
**FIG. 17.** Calculated imaginary bands of h-BN plotted against $k^2$, for a Schottky barrier.

transmission occurs by conventional tunneling at $E_F$. Now there is less spin filtering than in GGA, and possible TMR values return to values of typically $\sim$100%. These are shown in Fig. 18(b). The tunneling coefficients have also been calculated for other configurations (N on top, incommensurate, and for other sorption distances). Interestingly, if both electrodes have the evaporated $\sqrt{7} \times \sqrt{7}$ structure as in Figs. 10(c)–10(d), the TMR is increased to $10^3$% (theoretically). Thus, this configuration would be preferred in terms of spintronics, if it could be manufactured, as it is the less stable site.

As large TMR values are preferred, Faleev[74] noted that very large TMR values were possible for h-BN MTJs from his GGA bands using states lying within 0.6 eV of the h-BN valence band edge, where some spin-up polarized metal states are forbidden from tunneling across the barrier. In the GGA spin-polarized bands of Co in Fig. 12(a), spin-up states are absent in certain k ranges, and the spin-down states in Co are present close to $E_F$. (This is because of unusual behavior of the two evanescent states very close to the VBM.) Thus, it was noted there are spin-up states only for 0.6 eV below $E_F$ near the K point, whereas there are spin-down states only 0.2 eV below $E_F$ at the K point [circled in Fig. 12(a)]. This favors transmission by only the spin-down states, and it causes a large TMR value over this small energy range near the VBM. This result led to a focus on energies near the valence band edge of h-BN.

Faleev[74] showed that $E_F$ lay very close to the valence band edge, in the GGA bands. This effect was somewhat corrected in his more costly GW bands in which the h-BN VBM is lowered. However, the low speed of GW meant that a full TMR calculation could not be carried out. It was proposed that these lower energies near the VBM could still be accessed by a p-doping of the h-BN. Such doping in a wide gap material like h-BN is difficult but has been seen experimentally,[83] although it is absent theoretically in perfect crystals.[84] However, practically, such dopants would be fully ionized and such thin h-BN films would be fully depleted and unable to shift Ef.

An important question for h-BN barriers is their hexagonal lattice. Naganuma[85] has shown that PMA can be achieved experimentally for graphene on Fe MTJs using the L1$_0$-ordered tetragonal metal FePd as the electrode. The hexagonal graphene has been attached to L1$_0$-FePd electrodes to provide a mechanism for PMA.[74] During annealing, the L1$_0$-FePd adapts to the local quasi-hexagonal (111) arrangement of graphene during
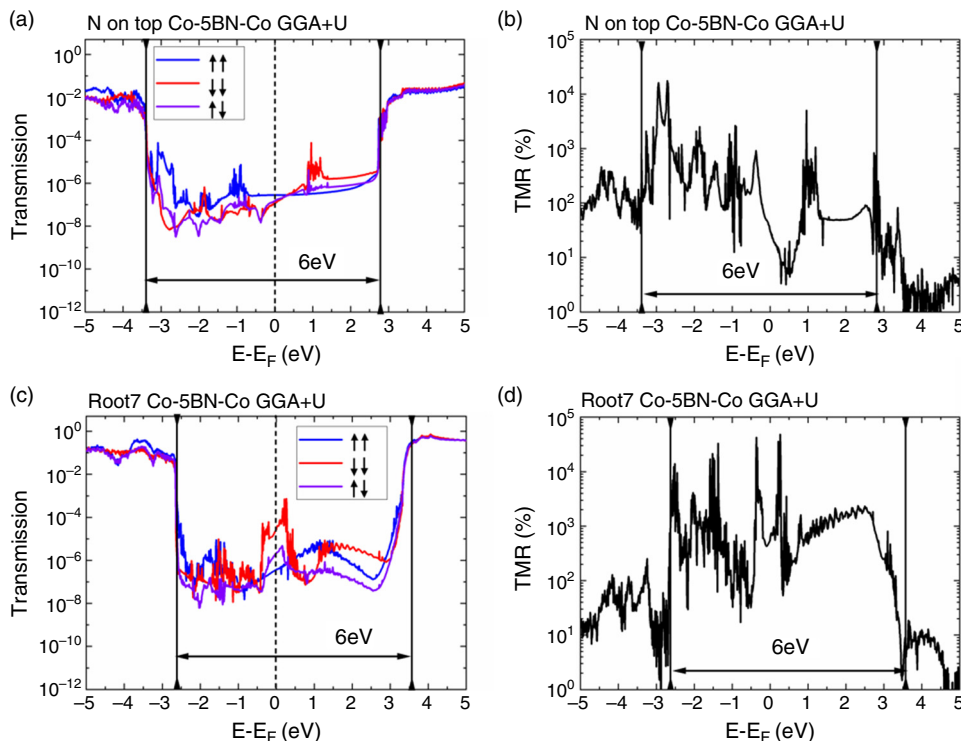


**FIG. 18.** (a) Transmission functions of various evanescent states across the tunnel barrier as a function of spin; (b) the overall calculated TMR for 5 layers of h-BN across the bandgap. [(c),(d)] Same for the $\sqrt{7} \times \sqrt{7}$ structure.

annealing, causing its contact layers to orient more toward the (111) direction, so it can provide a PMA effect.

Alternatively, h-BN on Fe or Co could secure a PMA using a hybridization mechanism, where there is a hybridization between the surface Co layer $d_z^2$ orbitals and N $p_z$ orbitals that shifts the empty spin-down Co $d_z^2$ state upward (and N pz state downwards), stabilizing the surface layer's filled N pz state, as in Fig. 19. This would generate a PMA. We see from the calculations in Fig. 19(a) that the interaction for the N-on-top site shifts the empty PDOS down-spin band of the surface Co layer at $+1$ eV upward, indicating that hybridization is occurring. This implies that there is a reciprocal downward shift of the occupied bonding state of N pz, and, thus, an increased bonding of the occupied states, giving the PMA. An equivalent shift of the empty surface Co layer is also seen in Figs. 19(b) and 19(c). However, it is less than for the layer 4 in red. This is because the hybridization is weaker due to the longer physisorption distance. Thus, the PMA effect is weaker for these sites. This applies not only for $\sqrt{7}$ sites but also for the B on top sites, where the Co must interact with the nearest N (occupied) site, not the B site directly below the Co site. Thus, there may be only sufficient PMA interaction when hBN is at the chemisorption site. Deposition of the top electrode should aim to provide this.

This PMA mechanism was recently observed experimentally on h-BN interfaces by Watanabe et al.[86] It could be stronger for chemisorbed hBN with shorter N-Co bond lengths, where the interaction is stronger. This mechanism would also supply PMA if the h-BN absorbed onto the metal in the B on top site. For the physisorption in the $\sqrt{7}$ structure, the surface N $p_z$ interacts with the symmetric combination of the $d_{x,y}$ orbitals of the surface Fe sites to supply a PMA. However, the interaction is much weaker for these bonds.

## DISCUSSION

So far experimentally, h-BN has been grown on the bottom metal layer by CVD requiring $\sim$900 °C, whereas the top metal layer was deposited by evaporation at 25 °C. This means that the bottom interface was chemisorbed, but the top interface was physisorbed; see Fig. 20. The effect of this on band offsets means that there is up to $\sim$2 eV potential difference between these electrodes. It would be preferable if both electrodes were the same type, but this requires common deposition methods. ALD can deposit h-BN on Ni down to 350 °C in some[54] but not all[52] reports. Similarly metals such as Co or Ni can be deposited by ALD recently[87–89] from 150 °C. This is against the culture of spintronics, but with a single deposition port ALD could be implemented, and changing deposition only requires a change of precursor gas and temperature, without breaking vacuum. The CVD temperature could also be lowered if this method is used. Thus, both interfaces would then be chemisorbed interfaces deposited at $\sim$350 °C, and there would be no voltage difference between electrodes. Or both interfaces should be deposited at 25 °C in the $\sqrt{7} \times \sqrt{7}$ structure, if this were possible.
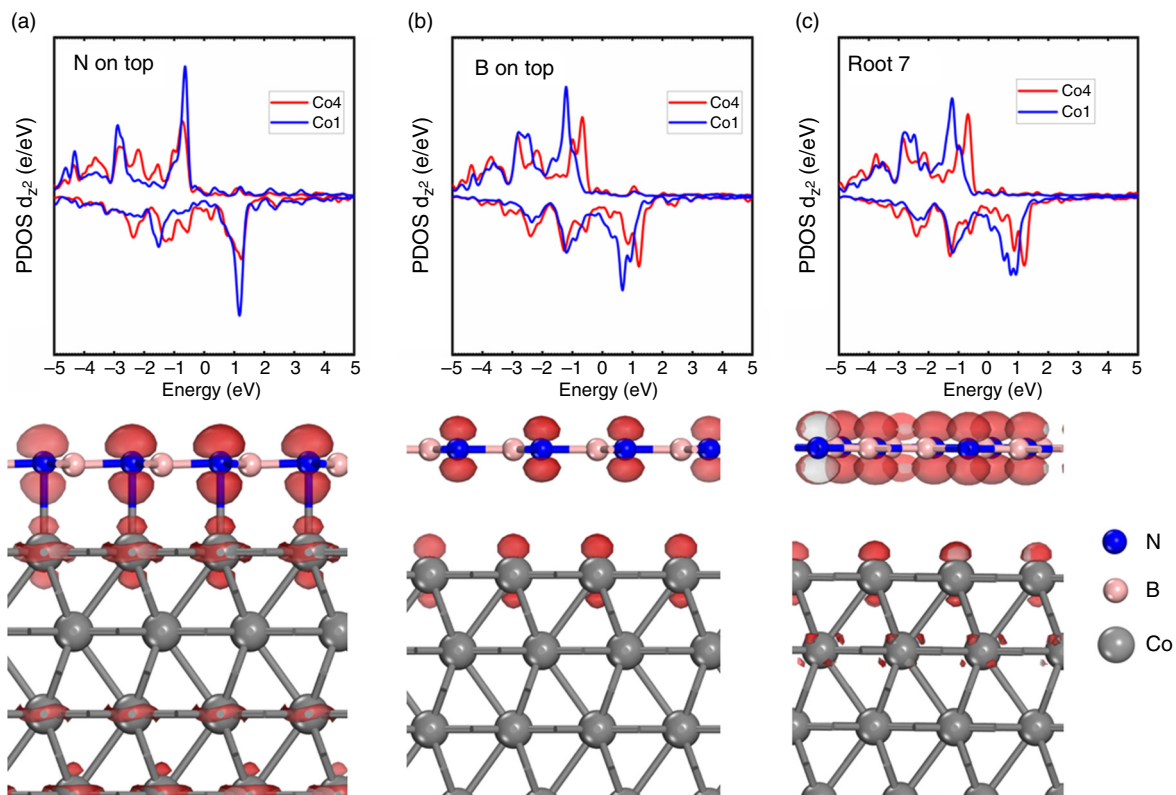


**FIG. 19.** Hybridization of the N $p_z$ orbital and the Co $d_{z2}$ orbital of the top Co layers, for N-on-top, B-on-top and incommensurate state. In (a)–(c), Co layer 1 is the interface, Co layer 4 is the central layer.
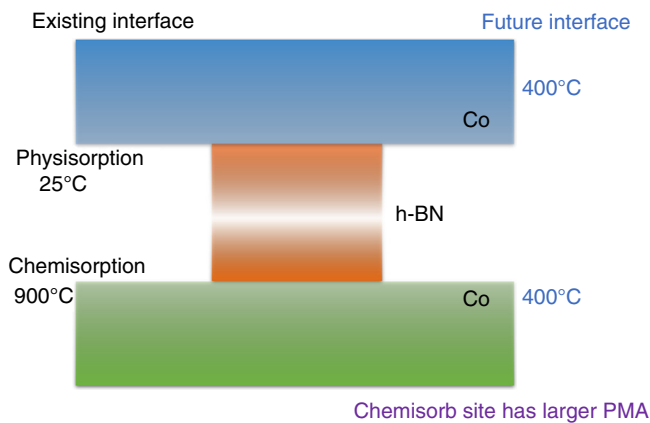
Existing interface                    Future interface

400°C

Co

Physisorption
25°C

h-BN

Chemisorption
900°C

Co                    400°C

Chemisorb site has larger PMA

**FIG. 20.** Co|h-BN interface type, (a) existing on left, (b) preferred on right.

Presently, the CVD temperature is kept high to give a large crystallite size in h-BN, for reasons often related to conduction in adjacent conductors.[45] The effect of h-BN grain size or h-BN short-range order on TMR is less studied and might have been larger than necessary for TMR reasons. MgO only has a ∼3–5 nm grain size in present textured layers. As long as h-BN is free of like-atom bonds, the TMR might be maintained. This would depend on short-range order, not grain size, and could be tested.

The above deposition of thin layers of ALD h-BN on Co or Ni(111) and the subsequent deposition of a Co or Ni electrode on top, giving a chemisorbed site, would provide sufficient TMR for a magnetic tunnel junction despite the basic symmetry being hexagonal rather than cubic. Although this symmetry does not have the more coherent evanescent s-like waves of the MgO cubic structure, there would still be some coherent tunneling via N $p_z$ states. Metallurgically, ALD would allow h-BN to grow at sufficiently low temperatures not to inject interstitial B atoms into the electrodes, while h-BN itself acts as a good diffusion barrier to metal atoms, as seen in its behavior when tested for low K dielectrics.[4]

Overall, there are considerable differences to using h-BN rather than MgO as the tunnel barrier. These are the very different deposition methods used for h-BN, the threefold symmetry of h-BN compared to the fourfold symmetry of MgO, and the unusual behavior the h-BN Schottky barrier height through the pillow effect. The symmetry change need not be so deleterious in that low temperature ALD deposition method can be used, which would conserve local order in chemical bonding of h-BN. This would conserve coherent tunneling for h-BN $p_z$ states across the barrier and so allow one tunneling mode to dominate. Another advantage of h-BN compared to MgO is that MgO is hygroscopic, whereas h-BN is not.

The problem for h-BN tunnel barriers is their hexagonal symmetry. The cubic symmetry of MgO allows other aspects of the tunnel junction to determine its ultimate scaling. With h-BN, there are many considerations such as the variation of TMR with contact type to consider that do not occur for cubic interfaces (Fig. 19). The relative simplicity of the cubic MgO|CoFe MTJs have allowed a roadmap for MTJ scaling to be planned to dimensions of 10 nm or less by being able to tolerate high aspect ratio structures for the top electrode, which can

still create a PMA.[9] On the other hand, the effect of hexagonal symmetry with PMA has not been fully explored.

An alternative cubic tunnel barrier of MgAl$_2$O$_4$ spinel has also been studied [90]. It contains both Al-O and Mg-O bonds. This has a good lattice match to Heusler alloys. It has the natural advantage of a cubic symmetry, but its TMR is lower than expected. There may be internal disorder of the Al atoms between the tetrahedral and octahedral spinel sites when quenching, which might lower the TMR.[90]

## CONCLUSIONS

Hexagonal boron nitride is studied as a possible tunnel barrier in magnetic tunnel junctions. It is argued that the present chemical vapor deposition process of h-BN should ideally be replaced by atomic layer deposition to lower the growth temperature, to a value that also minimizes B dissolution in the metal electrodes. The further development of ALD for both h-BN and the metal electrodes is argued to be beneficial to the testing and development of h-BN–based MTJs.

The fourfold interface symmetry of MgO-based tunnel barriers is contrasted with the hexagonal symmetry found in h-BN and (111) metal faces. Threefold symmetry is generally held to be disadvantageous because it can mix evanescent states of different orbital symmetries and, thus, leads to faster decay rates of evanescent states across the barrier, while the Δ1 mode of fourfold symmetry has the slowest decay rate. However, one Δ1 wave of threefold symmetry consists of s∗ states and also has a slower decay rate. Calculation finds that the TMR depends more strongly on energy across the bandgap in threefold systems, and there are unusual factors fixing the Fermi energy in the case of van de Waals systems. TMR is higher at the physisorbed distance between Co and the top h-BN layer. The closed shell of individual layers of h-BN means that the Schottky barriers depend on this distance by the "pillow effect," where the SBH depends strongly on whether the metal is chemisorbed or physisorbed to the layer and less on the work function of the specific metal. The use of a GGA+U calculation scheme on the h-BN self-energies allows us to simultaneously represent the Co and h-BN-like states correctly without the use of hybrid functional which distort metal states.

An interfacial perpendicular magneto-resistance (PMA) still exists in van der Waals insulator tunnel barriers using the Nakamura hybridization mechanism, which is critical to providing perpendicularly directed electrode spins. The possibility of $E_F$ lying close to the VBM as in some analyses, with the aim of obtaining very large TMR values, is suggested to be over-estimated and arises from fixing the metal-BN layer at too large a value and under-estimating the h-BN bandgap.

## ACKNOWLEDGMENTS

## DATA AVAILABILITY

The data that support the findings of this study are available from the corresponding author upon reasonable request.

## REFERENCES

[1] D. Akinwande, C. Huyghebaert, C. H. Wang, M. I. Serna, S. Goossens, L. J. Li, H. S. P. Wong, and F. H. L. Koppens, Nature **573**, 507 (2019).

[2] C. D. English, G. Shine, V. E. Dorgan, K. C. Saraswat, and E. Pop, Nano Lett. **16**, 3824 (2016).

[3] Y. Ji, C. Pan, M. Zhang, S. Long, X. Lian, F. Miao, F. Hui, Y. Shi, L. Larcher, E. Wu, and M. Lanza, App. Phys. Lett. **108**, 012905 (2016).

[4] S. Hong, C. S. Lee, M. H. Lee, Y. D. Lee, K. Y. Ma, G. Kim, S. I. Yoon, K. J. Kim, S. W. Kim, E. C. Jeon, H. Jeon, H. I. Lee, Z. Lee, A. Antidormi, S. Roche, M. Chhowalla, H. J. Shin, and H. S. Shin, Nature **582**, 511 (2020).

[5] R. Ge, X. Wu, M. Kim, J. Shi, S. Sonde, L. Tao, Y. Zhang, J. C. Lee, and D. Akinwande, Nano Lett. **18**, 434 (2017); X. Wu, R. Ge, P.-A. Chen, H. Chou, Z. Zhang, Y. Zhang, S. Banerjee, M.-H. Chiang, J. C. Lee, and D. Akinwande, Adv. Mater. **31**, 1806790 (2019).

[6] Y. Shi, X. Liang, B. Yuan, V. Chen, H. Li, F. Hui, Z. Yu, F. Yuan, E. Pop, H. S. P. Wong, and M. Lanza, Nat. Elec. **1**, 458 (2018).

[7] S. Yuasa, K. Hono, G. Hu, and D. C. Worledge, MRS Bull. **43**, 352 (2018); A. D. Kent and D. C. Worledge, Nat. Nano. **10**, 187 (2015).

[8] S. Miura, K. Nishioka, H. Naganuma, T. V. A. Nguyen, H. Honjo, S. Ikeda, T. Watanabe, H. Inoue, M. Niwa, T. Tanigawa, Y. Noguchi, T. Yoshizuka, M. Yasuhira, and T. Endoh, IEEE Trans. Electron Devices **67**, 5368 (2020).

[9] B. Jinnai, K. Watanabe, S. Fukami, and H. Ohno, App. Phys. Lett. **116**, 160501 (2020).

[10] S. Yuasa, T. Nagahama, A. Fukushima, Y. Suzuki, and K. Ando, Nat. Mater. **3**, 868 (2004).

[11] S. Yuasa and D. D. Djayaprawira, J. Phys. D **40**, R337 (2007); S. Yuasa, *Intermag Conf* (IEEE, 2012).

[12] J. Hayakawa, S. Ikeda, F. Matsukura, H. Takahashi, and H. Ohno, Jpn. J. App. Phys. **44**, L587 (2005).

[13] S. Mangin et al., Nat. Mat. **5**, 210 (2006).

[14] M. Endo, S. Kanai, S. Ikeda, F. Matsukura, and H. Ohno, App, Phys, Lett. **96**, 212503 (2010).

[15] S. Ikeda, K. Miura, H. Yamamoto, K. Mizunuma, H. D. Gan, M. Endo, S. Kanai, J. Hayakawa, F. Matsukura, and H. Ohno, Nat. Mat. **9**, 721 (2010).

[16] K. Watanabe, B. Jinnai, S. Fukami, H. Sato, and H. Ohno, Nat. Comm. **9**, 663 (2018).

[17] Z. Wang, M. Saito, K. P. McKenna, S. Fukami, H. Sato, S. Ikeda, H. Ohno, and Y. Ikuhara, Nano Lett. **16**, 1530 (2016).

[18] W. H. Butler, X. G. Yang, T. C. Schulthess, and J. M. Maclaren, Phys. Rev. B **63**, 054416 (2001).

[19] J. Chen, Z. Zhang, Y. Guo, and J. Robertson, J. App. Phys. **129**, 175304 (2021).

[20] A. Schleife, C. Rödl, F. Fuchs, J. Furthmüller, and F. Bechstedt, Phys. Rev. B **80**, 035112 (2009).

[21] N. W. Ashcroft and N. D. Mermin, *Solid State Physics* (Holt-Saunders Int. Ed. 1976), p. 335.

[22] H. X. Yang, M. Chishiev, B. Dieny, J. H. Lee, A. Manchon, and K. H. Shin, Phys. Rev. B **84**, 054401 (2011).

[23] H. Naganuma, G. Kim, Y. Kawada, N. Inami, K. Hatekyama, S. Iihama, K. M. Nazrul-Islam, M. Oogane, S. Mizkami, and Y. Ando, Nano Lett. **15**, 623 (2015); F. Wu, S. Mizukami, D. Watanabe, H. Naganuma, M. Oogane, Y. Ando, and T. Miyazaki, Appl. Phys. Lett. **94**, 122503 (2009); M. Hosoda, M. Oogane, M. Kubota, T. Kubota, H. Saruyama, S. Iihama, H. Naganuma, and Y. Ando, J. Appl. Phys. **110**, 013915 (2011).

[24] K. Nakamura, T. Akiyama, T. Ito, M. Weinert, and A. J. Freeman, Phys Rev B **81**, 220409(R) (2010).

[25] R. Shimabukuro, K. Nakamura, T. Akiyama, and T. Ito, Phys. E **42**, 1014 (2010).

[26] M. Yamanouchi, R. Koizumi, S. Ikeda, H. Sato, K. Mizunuma, K. Miura, H. D. Gan, F. Matsukura, and H. Ohno, J. Appl. Phys. **109**, 07C712 (2011).

[27] A. H. Castro Neto, F. Guinea, N. M. R. Peres, K. S. Novoselov, and A. K. Geim, Rev. Mod. Phys. **81**, 109 (2009).

[28] B. Arnaud, S. Lebegue, P. Rabiller, and M. Alouani, Phys. Rev. Lett. **96**, 026402 (2006).

[29] A. Catellani, M. Posternak, A. Baldereschi, H. F. Jansen, and A. J. Freeman, Phys. Rev. B **32**, 6997 (1985).

[30] H. Medina, Y. C. Lin, C. Jin, C. C. Lu, C. H. Yeh, K. P. Huang, K. Suenaga, J. Robertson, and P. W. Chiu, Adv. Func. Mat. **22**, 2123 (2012).

[31] X. Li, W. Cai, J. An, S. Kim, J. Nah, D. Yang, R. Piner, A. Velamakanni, E. Tutuc, S. K. Banerjee, L. Colombo, and R. S. Ruoff, Science **324**, 1312 (2009).

[32] S. Hofmann, P. Braeuninger-Weimer, and R. S. Weatherup, J. Phys. Chem. Lett. **6**, 2714 (2015).

[33] S. Rahimi, L. Tao, S. Chowdhury, S. Park, A. Jouvray, S. Buttress, N. Rupesinghe, K. Teo, and D. Akinwande, ACS Nano **8**, 10471 (2014).

[34] G. F. Zhong, X. Y. Wu, L D'Arsié, K. Teo, N. L. Rupesinghe, A. Jouvray, and J. Robertson, App. Phys. Lett. **109**, 193103 (2016); X. Wu, G. Zhong, L. D'Arsié, H. Sugime, S. Esconjaregui, A. W. Robertson, and J. Robertson, Sci. Rep. **6**, 21152 (2016).

[35] J. Robertson, J. Mat. Chem. **22**, 19858 (2012).

[36] K. F. Mak, C. Lee, J. Hone, J. Shan, and T. F. Heinz, Phys. Rev. Lett. **105**, 136805 (2010).

[37] S. M. Eichfeld, L. Hossain, Y. C. Lin, A. F. Piasecki, B. Kupp, A. G. Birdwell, N. Lu, X. Peng, J. Li, A. Azcatl, S. McDonnell, R. M. Wallace, M. J. Kim, T. S. Mayer, J. M. Redwing, and J. A. Robinson, ACS Nano **9**, 2080 (2015).

[38] R. Y. Yue, Y. Nie, L. A. Walsh, R. Addou, C. Liang, N. Lu, A. T. Barton, H. Zhu, Z. Che, D. Barrera, L. Cheng, P. R. Cha, Y. J. Chabal, J. Hsu, J. Kim, L. Colombo, R. M. Wallace, K. Cho, and C. L. Hinkle, 2D Mater. **4**, 045019 (2017).

[39] D. Chiappe et al., Nanotechnology **29**, 425602 (2018).

[40] Y. Guo, D. Liu, and J. Robertson, App. Phys. Lett. **106**, 173106 (2015).

[41] C. Gong, L. Colombo, R. M. Wallace, and K. J. Cho, Nano Lett. **14**, 1714 (2014).

[42] C. M. Smyth, R. Addou, S. McDonnell, C. L. Hinkle, and R. M. Wallace, J. Phys. Chem. C **120**, 14719 (2016).

[43] Y. Guo, D. Liu, and J. Robertson, ACS App. Mater. Interfaces **7**, 25709 (2015).

[44] C. R. Dean, A. F. Young, I. Meric, C. Lee, L. Wang, S. Sorgenfrei, K. Watanabe, T. Taniguchi, P. Kim, K. L. Shepard, and J. Hone, Nat. Nano **5**, 722 (2010).

[45] S. Caneva, R. S. Weatherup, B. C. Bayer, R. Blume, A. Cabrero-Vilatela, P. B. Weimer, M. B. Martin, R. Wang, C. Baehtz, R. Schloegl, J. C. Meyer, and S. Hofmann, Nano Lett. **16**, 1250 (2016).

[46] R. S. Weatherup, B. Dlubak, and S. Hofmann, ACS Nano **6**, 9996 (2012); P. R. Kidami, C. Ducati, B. Dlubak, D. Gardiner, R. S. Weatherup, M. B. Martin, P. Seneor, H. Coles, and S. Hofmann, J. Phys. Chem. C **116**, 22492 (2012);

[47] A. C. Vilatela, R. S. Weatherup, P. Braeuninger, S. Caneva, and S. Hofmann, Nanoscale **8**, 2149 (2016).

[48] A. Ismach, H. Chou, D. A. Ferrer, Y. Wu, S. McDonnell, H. C. Floresca, A. Covacevich, R. Piner, M. J. Kim, R. M. Wallace, L. Colombo, and R. S. Ruoff, ACS Nano **6**, 6378 (2012).

[49] S. Caneva et al., ACS App. Mat. Interfaces **9**, 29973 (2017).

[50] C. Jin, F. Lin, K. Suenaga, and S. Iijima, Phys. Rev. Lett. **102**, 195505 (2009).

[51] S. M. Kim, A. Hsu, M. H. Park, S. H. Chae, S. J. Lee, D. H. Cho, W. Fang, C. Lee, T. Palacios, M. Dresselhaus, K. K. Kim, Y. H. Lee, and J. Kong, Nat. Comm. **16**, 9662 (2015).

[52] J. Lee, A. V. Ravichandran, J. Mohan, L. Cheng, A. T. Lucero, H. Zhu, Z. Che, M. Catalano, M. J. Kim, R. M. Wallace, A. Venugopal, W. Choi, L. Colombo, and J. Kim, ACS App. Mat. Interfaces **12**, 36688 (2020).

[53] S. Wolf, M. Edmonds, K. Sardashti, M. Clemons, J. H. Park, N. Yoshida, L. Dong, S. Nemani, E. Yieh, R. Holmes, D. Alvarez, and A. Kummel, App. Surf. Sci. **439**, 689 (2018).

[54] J. Jones, A. Pilli, V. Lee, J. Beatty, and B. Beauclair, J Vac Sci Technol A **37**, 060903 (2019).

[55] J. Jones, B. Beauclair, and O. Olanipekun, J Vac Sci Technol A **35**, 01B139 (2017).

[56] M. S. Driver, J. D. Beatty, O. Olanipekun, K. Reid, A. Rath, P. M. Voyles, and J. A. Kelber, Langmuir **32**, 2601 (2016).

[57] H. M. Naguib and R. Kelly, Rad. Eff. **25**, 1 (1975); K. Trachenko, J. M. Pruneda, E. Artacho, and M. T. Dove, Phys. Rev. B **71**, 184104 (2005).

[58] B. F. Levine, J. Chem. Phys. **59**, 1463 (1973).

[59] A. L. Gibb, N. Alem, J. H. Chen, K. J. Erickson, J. Ciston, A. Gautam, M. Linck, and A. Zettl, J Am. Chem. Soc. **135**, 6758 (2013).

[60] Q. Li, X. Zou, M. Liu, J. Sun, Y. Gao, Y. Qi, X. Zhou, B. L. Yakobson, Y. Zhang, and Z. Liu, Nano Lett. **15**, 5804 (2015).

[61]H. Lu, Y. Guo, J. W. Martin, M. Kraft, and J. Robertson, Carbon **147**, 483 (2019).

[62]A. Ebnonnasir, S. Kodambaka, and C. V. Ciobanu, Surf. Sci. Rev. Lett. **22**, 1650078 (2015).

[63]A. Nagashima, N. Tejima, Y. Gamou, T. Kawai, and C. Oshima, Phys. Rev. Lett. **75**, 3918 (1995).

[64]J. Ontaneda, F. Viñes, F. Illas, and R. Grau-Crespo, Phys. Chem. Chem. Phys. **21**, 10888 (2019).

[65]M. Bokdam, G. Brocks, M. J. Katnelson, and P. J. Kelly, Phys. Rev. B **90**, 085415 (2014).

[66]S. Grimme, J. Comp. Chem. **27**, 1787 (2006); J. Chem. Phys. **132**, 154104 (2010).

[67]S. J. Clark and J. Robertson, Phys. Rev. B **82**, 085208 (2010).

[68]J. Robertson, Phys. Rev. B **29**, 2131 (1984).

[69]S. Ogawa, T. Yamada, R. Kadowaki, T. Taniguchi, T. Abukawa, and Y. Takakuwa, J. App. Phys. **125**, 144303 (2019); K. P. Loh, I. Sakaguchi, M. N. Gamo, S. Tagawa, T. Sugino, and T. Ando, App. Phys. Lett. **74**, 28 (1999).

[70]D. Y. Usachov *et al.*, Phys. Rev. B **98**, 195438 (2018).

[71]H. Vazquez, Y. J. Dappe, J. Ortega, and F. Flores, J. Chem. Phys. **126**, 144704 (2007).

[72]H. Vázquez, R. Oszwaldowski, P. Pou, J. Ortega, R. Perez, F. Flores, and A. Kahn, Europhys. Letts. **65**, 802 (2004).

[73]J. Hwang, A. Wan, and A. Kahn, Mater. Sci. Eng. R Rep. **64**, 1 (2009).

[74]S. V. Faleev, S. Parkin, and O. N. Mryasov, Phys. Rev. B **92**, 235118 (2015).

[75]B. Dlubak, M. B. Martin, R. S. Weatherup, H. Yang, C. Deranlot, R. Blume, R. Schlogl, A. Anane, S. Hofmann, P. Seneor, and J. Robertson, ACS Nano **6**, 10930 (2012); M. B. Martin, B. Dlubak, R. S. Weatherup, H. Yang, C. Deranlot, K. Bouzehouane, F. Petroff, A. Anane, S. Hofmann, J. Robertson, A. Fert, and P. Seneor, ACS Nano **8**, 7890 (2014); M. Piquemal-Banci, R. Galceran, S. Caneva, M. B. Martin, R. S. Weatherup, P. R. Kidambi, K. Bouzehouanne, S. Xavier, A. Anane, F. Petroff, J. Robertson, S. Hofmann, B. Dlubak, and P. Seneor, App. Phys. Lett. **108**, 102404 (2016).

[76]M. Piquemal-Banci, R. Galceran, F. Godel, S. Caneva, M. B. Martin, R. S. Weatherup, P. R. Kidambi, K. Bouzehouane, S. Xavier, A. Arane, F. Petroff, A. Fert, S. Mutien-Marie Dubois, J. C. Charlier, J. Robertson, S. Hofmann, B. Dublak, and P. Seneor, ACS Nano **12**, 4712 (2018).

[77]M. Picquemal-Banci, R. Galceran, M. B. Martin, F. Godel, A. Anane, F. Petroff, B. Dlubak, and P. Seneor, J. Phys. D **50**, 293002 (2017).

[78]A. Dankert, M. V. Kamalakar, A. Wajid, R. S. Patel, and S. P. Dash, Nano Res. **8**, 1357 (2015).

[79]H. Yang, A. D. Vu, A. Hallal, N. Rougemaille, J. Cotaux, G. Chen, A. K. Schmid, and M. Chshiev, Nano Lett. **16**, 145 (2016).

[80]V. M. Karpan, G. Giovannetti, P. A. Khomyakov, M. Talanana, A. A. Starikov, M. Zwierzycki, J. van der Blink, G. Brocks, and P. J. Kelly, Phys. Rev. Lett. **99**, 176602 (2007).

[81]V. M. Karpan, P. A. Khomyakov, G. Giovannetti, A. A. Starikov, and P. J. Kelly, Phys. Rev. B **84**, 153406 (2011).

[82]M. Bokdam, G. Brocks, M. I. Katsnelson, and P. J. Kelly, Phys. Rev. B **90**, 075415 (2014).

[83]H. X. Jiang and J. Y. Lin, Semicond. Sci. Technol. **29**, 084003 (2014).

[84]L. Weston, D. Wickramarante, and C. G. van de Walle, Phys. Rev. B **96**, 100102(R) (2017).

[85]H. Naganuma, V. Zatko, M. Galbiati, F. Godel, A. Sander, C. Carretero, O. Bezencenet, N. Reyren, M. B. Martin, B. Dlubak, and P. Seneor, App. Phys. Lett. **116**, 173101 (2020).

[86]T. Watanabe, Y. Yamada, A. Koide, S. Entani, S. Li, Z. I. Popov, P. B. Sorokin, H. Naramoto, M. Sasaki, K. Amemiya, and S. Sasaki, App. Phys. Lett. **112**, 022407 (2018).

[87]M. F. J. Vos, G. van Straaten, W. M. M. E. Kessels, and A. J. M. Mackus, J. Phys. Chem. **122**, 22519 (2018).

[88]M. Kim, S. Nabeya, D. K. Nandi, K. Suzuki, H. M. Kim, S. Y. Cho, K. B. Kim, and S. H. Kim, ACS Omega **4**, 11126 (2019).

[89]M. M. Kerrigan, J. P. Klesko, S. M. Rupich, C. L. Dezelah, R. K. Kanjolia, Y. J. Chabal, and C. H. Winter, J. Chem. Phys. **146**, 052813 (2017).

[90]M. Belmoubarik, H. Sukegawa, T. Ohkubo, S. Mitani, and K. Hono, App. Phys. Lett. **108**, 132404 (2016); K. Nawa, K. Masuda, and Y. Miura, Phys. Rev. B **102**, 144423 (2020); K. Masuda and Y. Miura, Phys. Rev. B. **96**, 054428 (2017).